International Journal of Fatigue 164 (2022) 107146

Contents lists available at ScienceDirect

International Journal of Fatigue

journal homepage: www.elsevier.com/locate/ijfatigue

Mechanical characterization and fatigue assessment of wire and arc additively manufactured HSLA steel parts

Nicolae Rodideal [a], Carla M. Machado [b], Virgínia Infante [c], Daniel F.O. Braga [c], Telmo G. Santos [b], Catarina Vidal [b,*]

[a] Department of Mechanical and Industrial Engineering, NOVA School of Science and Technology, Universidade Nova de Lisboa, 2829-516 Caparica, Portugal
[b] UNIDEMI, Department of Mechanical and Industrial Engineering, NOVA School of Science and Technology, Universidade Nova de Lisboa, 2829-516 Caparica, Portugal
[c] LAETA, IDMEC, Instituto Superior Técnico, Universidade de Lisboa, Av. Rovisco Pais 1, 1049-001 Lisbon, Portugal

ARTICLE INFO

Keywords:
HSLA steel
Wire and Arc Additive Manufacturing (WAAM)
Non-Destructive Testing (NDT)
Mechanical properties
Fatigue

ABSTRACT

Wire and arc additive manufacturing (WAAM) has been attracting industrial attention due to its high productivity and flexibility. However, fatigue life data of WAAM HSLA steel is scarce. In this study, the mechanical properties and fatigue life of thin-walled HSLA steel parts fabricated by WAAM were assessed via non-destructive and destructive testing, providing a comprehensive analysis on this material's behaviour. The manufacturing conditions have a more pronounced effect on mechanical properties than the part's height, which seems not to influence the fatigue life of WAAM HSLA steels.

1. Introduction

Industry is moving towards a new concept of manufacturing where sustainability plays an important role [1]. The 4th Industrial Revolution, or Industry 4.0, combines the technological achievements from the past years with a vision of future intelligent and automated production systems [2]. Over the years, the increase in product customization, geometry complexity and short lead time demands, forced the existing manufacturing systems to readapt to meet such requirements. Thus, additive manufacturing (AM) presents itself as a key technology since it can create complex components using a layer-by-layer material deposition. Wire and arc additive manufacturing (WAAM) has become a promising alternative to conventional machining. WAAM offers high deposition rates, high quality, and the feasibility of using materials that are otherwise difficult to process [3].

As WAAM progressively sees its development in the manufacturing industry, more studies have been conducted regarding process conditions and how they influence the mechanical properties, thermal history and residual stresses of different materials fabricated by this technology. With the constant advance of technology, AM processes evolved and began being used to produce patterns, tooling, and final parts. Currently, AM products and services are used in several activities, including energy, transportation, manufacturing, art, architecture, space exploration, and defense [4].

Suryakumar et al. [5] studied the correlation between thermal cycles and hardness along the building direction on a carbon steel ER70S-6 using a Gas Metal Arc Welding (GMAW) - based hybrid layered manufacturing process and concluded that the number of layers influence the hardness of the part. Haden et al. [6] investigated mechanical properties of two steels, stainless steel 304 and mild steel ER70S comparing with their wrought parts. For stainless steel, yield tensile strength (YTS) values exceeded those of the wrought part and varied both according to the welding direction and height. Ultimate tensile strength (UTS) results, on the other hand, were similar to the wrought part, suggesting that thermal history has a greater impact in YTS than UTS. As for the mild steel, both YTS and UTS are similar to the wrought parts. Alberti el al. [7] studied the material behaviour on a substrate with and without pre-heating, concluding that the latter resulted in a homogeneous temperature distribution, lower temperature gradients, reduced thermal stresses and improved wettability and consequently improved mechanical properties. The maximum temperature achieved in each layer has a direct influence in the subsequent layer, i.e., the first layer melts and solidifies onto the substrate, once the second layer is deposited, introducing more heat, partially melting the previous layer and itself. This has implications in grain distribution and overall mechanical properties [8,9].

High–strength low–alloy (HSLA) steels are structural materials initially developed to replace low–carbon steels due to their strength-to-

* Corresponding author at: NOVA School of Science and Technology, Universidade Nova de Lisboa, Portugal.
E-mail address: c.vidal@fct.unl.pt (C. Vidal).

https://doi.org/10.1016/j.ijfatigue.2022.107146
Received 14 March 2022; Received in revised form 28 June 2022; Accepted 12 July 2022
Available online 16 July 2022

Table 1
Chemical composition of the ER110S-G wire electrode [34].

Element	C	Mn	Si	Ni	Cr	Mo	Fe
wt.%	0.10	1.70	0.70	2.0	0.30	0.50	Balance

Table 2
Mechanical properties of the ER110S-G wire electrode [34].

Yield Strength (MPa)	Tensile Strength (MPa)	Elongation (%)	Impact ISO-V (J)
880 – 920	940 – 980	16 – 20	65 – 95

Table 3
Manufacturing parameters [12].

Sample	Voltage (V)	Current (A)	Wire feed speed (mm/s)	Travel Speed (mm/s)	Heat input (J/mm)
Low heat input (1L, 2L, 3L, 7L, 8L, 9L)	21	95	3	9	221
High heat input (4H, 5H, 6H)				3.9	511

weight ratio. HSLA steels have high strength, high ductility, high fracture toughness at low temperature, higher weldability and reduced heat affected zones when compared to other high strength steels [10,11]. Research regarding thermal cycles during manufacturing was carried out by Rodrigues et al. [12] on HSLA thin-walled parts, using high heat input and low heat input specimens. It was observed that microhardness depends on the heat input, being higher and more uniform for low heat input levels, while surface waviness (measurement of the more widely spaced part of surface texture) decreased when used high heat input. As for uniaxial tensile strength both specimens presented similar results, with high UTS and ductility. Further literature review suggests that most of the work done to date focuses primarily on material microstructure, tension/compressive testing. Moreover, very little published data exists regarding properties such as fracture toughness, fatigue strength or fatigue crack growth rate [13–15]. As to HSLA steels, there is still a lack of research related to WAAM.

Fatigue behaviour of structures and parts is of major concern in industry. With special attention to WAAM technology, research has to be developed in order to evaluate how components behave under different environmental and loading conditions [15]. So far, a few studies were carried out regarding the fatigue life relationship with porosity defects and crack initiation [16–23]. Gordon et al. [19] investigated the crack growth using 304L austenitic stainless steel for specimens parallel and perpendicular to the building direction. Results were correlated to microstructure, residual stresses, and texture. It was observed that the building direction has influence on the fatigue behaviour, since vertical specimens showed better fatigue resistance. The differences between horizontal and vertical results were attributed to long columnar grains and strong texture in the building direction. Subsequently, compressive residual stresses showed to slow down fatigue crack growth rate when compared to stress relieved specimens [16]. Altogether, comparing with wrought 304L parts, the as-built specimens showed similar/increased results regarding fatigue performance.

Zhang et al. investigated crack growth rate and fracture toughness on

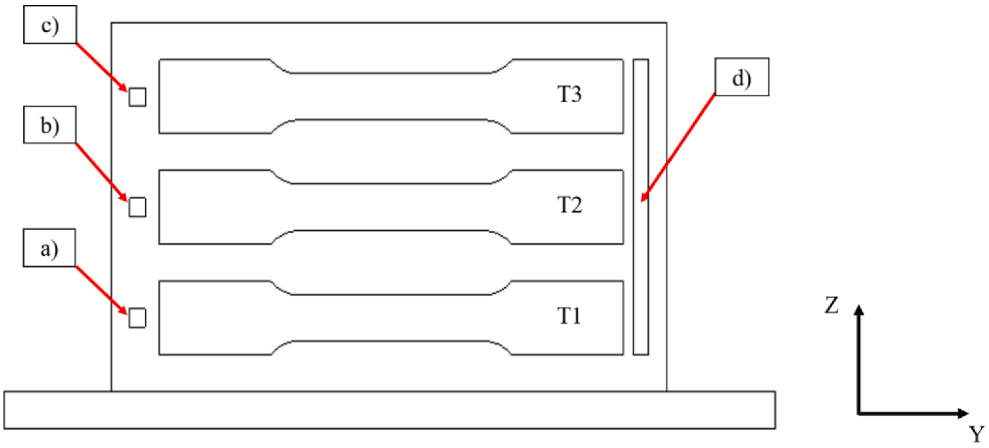

Fig. 1. Schematic representation of specimens (T1, T2 and T3) and samples (a), b), c) and d)) location.

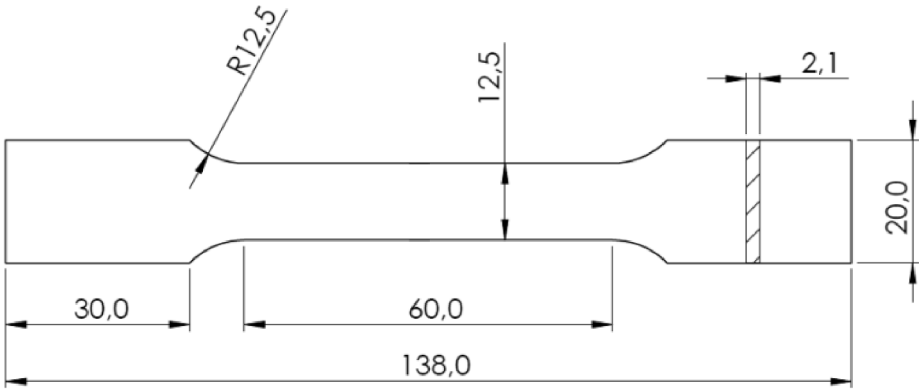

Fig. 2. Dimensions of the uniaxial tensile test specimens.

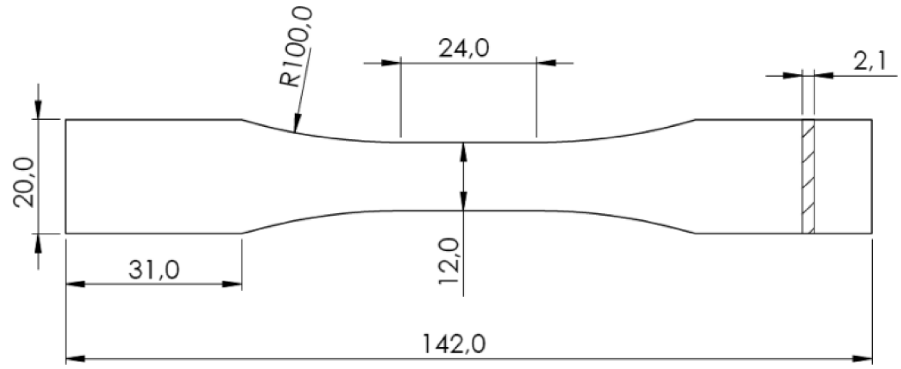

Fig. 3. Dimensions of the fatigue test specimens.

Table 4
Waviness and width average values of each sample type.

Sample	Waviness (μm)	Width (mm)
Low heat input	597 ± 88	4.9 ± 0.2
High heat input	660 ± 143	8.2 ± 0.3

Ti-6Al-4V WAAM processed parts [18]. Focusing on microstructure and residual stresses, the study concluded that crack growth rate is smaller when compared to wrought parts and has a tortuous path. This occurs mainly because of the lamellar structure present in WAAM, whereas the wrought alloy has an equiaxed grain distribution producing a straight and smooth crack. The effect of residual stresses depends on the crack location and direction. As for porosity, Biswal et al. [20] carried out a study where two types of specimens of Ti-6Al-4V were compared. One group without porosity and another with designed porosity. It was observed that although static strength remained similar, specimens with porosity had a 60% elongation reduction and a 33% lower fatigue strength comparing to the specimens without porosity.

An investigation conducted by Wachter et al. [24] aimed to determine the influence of inter layer temperature on material properties. Monotonic and cyclic testing was performed, as well as residual stresses were measured, on a medium strength steel material designed to weld HSLA structural steels. Specimens from different regions were extracted and tested. It was observed that residual stresses tend to be higher and tensile in the top region and more of compressive in middle and bottom regions. Tensile strength results do not present significant variation, except for YTS, which was higher on the lower interlayer temperature samples. Regarding fatigue results, no pronounced trend was recognized, although, it was noted that the heat treatment led to compression-dominated residual stresses at the surface, which delayed fatigue failure that is known to be initiated in this region.

In the recent past, several researchers have studied the fatigue behaviour of WAAM parts [25–33], showing that this is a topic of scientific and industrial relevance. Xin et al. [25] and Li et al. [26] studied the fatigue life performance of WAAM stainless steels. In [25] the results showed that the fatigue performance of structural steel is better than that of the WAAM stainless steel and the fatigue performance of vertical to printing direction is better than that along the printing direction. In [26], the WAAM specimens showed slightly higher fatigue life at relatively high strain amplitudes when compared to the hot-rolled counterparts, but lower fatigue resistance at low strain amplitudes, which is justified by the crack initiation and higher crack propagation resistance. Ermakova et al. [27,28] performed fatigue crack growth rate tests on ER70S-6 low carbon steel WAAM components. The experimental results were compared to the recommended trends in BS7910 standard. Xie et al. [29] and Liao et al. [30] investigated the fatigue resistance of Al-Mg4.5Mn alloy produced by hybrid situ rolled wire and arc additive

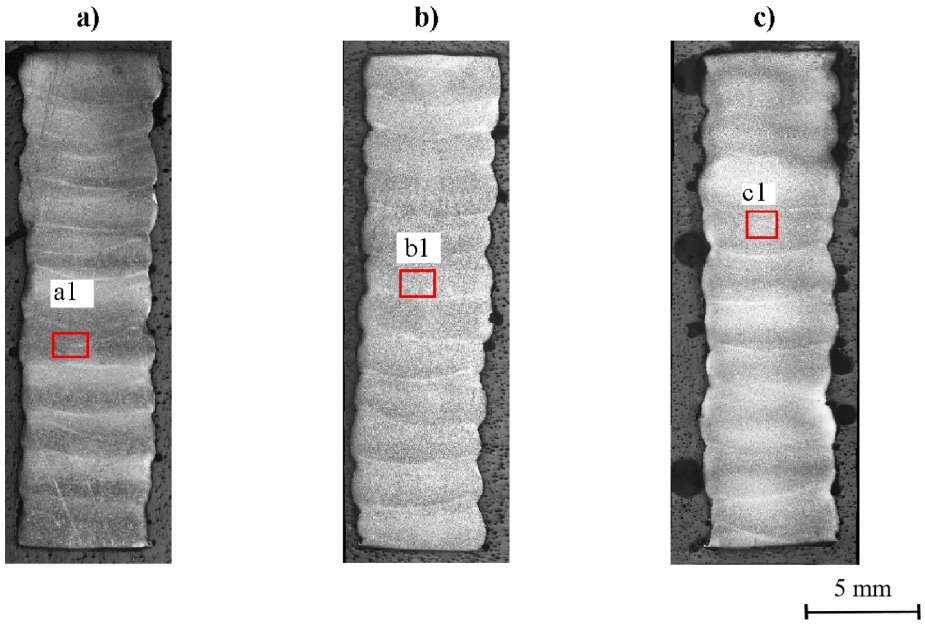

Fig. 4. Macrographs of low heat input samples across a) bottom, b) middle and c) top regions.

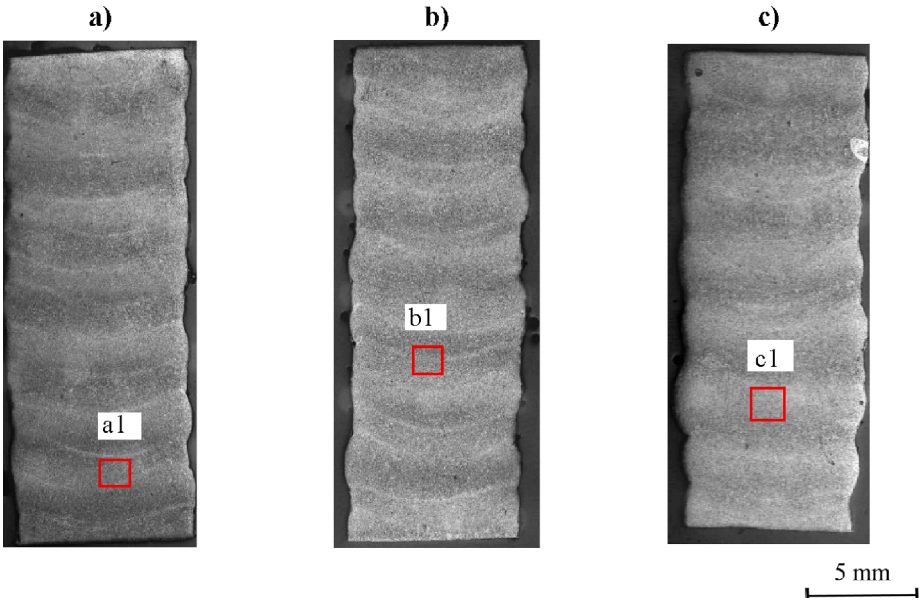

Fig. 5. Macrographs of high heat input samples across a) bottom, b) middle and c) top regions.

manufacturing. The results show superior tensile and fatigue properties due to a grain retirement compared to standard WAAM. Syed et al. [31], Wang et al. [32] and Akgun et al. [33] also investigated the fatigue behaviour of WAAM Ti-6Al-4V alloy specimens. Results showed different tensile and fatigue properties related with specimens and manufacturing orientation, grain and process-induced defects. A study conducted by Syed et al. [31] reports a fatigue strength of 600 MPa for 10^7 cycles concerning oscillation built vertical samples and parallel pass build orientations. The fractography analysis showed that most of the samples present crack initiation from pores. Also, Wang et al. [32] presented an investigation quantifying the inter- and trans-granular crack growth rates. Akgun et al. [33] showed that defects promote premature failure and dispersion on fatigue behaviour results.

With this study, the authors aimed to contribute to the development of the WAAM technology as far as fatigue life of WAAM HSLA steel parts is concerned. The microhardness, magnetic permeability and electrical conductivity of the WAAM HSLA steel parts were measured and related with the microstructure. Furthermore, mechanical properties along the parts' height were assessed for two different manufacturing heat input conditions and fatigue tests were carried on low heat input specimens.

2. Materials and methods

2.1. Materials

The wire electrode used to produce the additive manufactured parts was a commercial HSLA steel, AWS A5.28 ER110S-G, of 1 mm-diameter purchased from Dratec Drahttechnik GmbH. Its chemical composition and mechanical properties are described in Tables 1 and 2, respectively. Mild steel plates with dimensions of 250x100x10 mm were used as the substrate.

2.2. Production of the additive manufactured HSLA steel parts

Thin-walled wire and arc additive manufactured HSLA steel parts were produced using a custom-built welding torch mounted on a three-axis positioning system, a *KEMPY* welding machine with a power source Pro MIG 3200, wire feeder and control unit Pro MIG 501. Inverse polarity (DCEP/DC+) was also used. A zig-zag deposition strategy was employed as described in [35]. A contact-tip-to-work distance (CTWD) of 7 mm, a dwell time between layers of 1 min and a shielding gas (Ar 99.999%) at a flow rate of 12 L/min were used and kept constant in all depositions. The parts' dimensions were set to 180 mm in length and 100 mm in height. The WAAM deposition parameters used to manufacture the parts are listed in Table 3 and were those employed in [12]. Parts were fabricated with two different heat inputs by varying the travel speed.

As similar HSLA steel parts produced by WAAM did not reveal a uniform behaviour along its height during milling operations [35], the present study aimed to evaluate the mechanical properties along the thin-walled parts height owing to understand the differences reported. Therefore, specimens for tensile and fatigue testing (T1, T2 and T3), as well as samples for microstructure analysis (a), b) and c)), microhardness, magnetic permeability and electrical conductivity measurements (d)) were taken from three different locations (bottom, middle and upper regions) as illustrated in Fig. 1.

2.3. Characterization of the HSLA steel parts produced by WAAM

2.3.1. Surface waviness measurements

Surface waviness measurements were performed on the additive manufactured HSLA steel parts according to the procedure described in [36], by averaging the difference between the maximum wall width and the effective wall width. After all parts produced being scanned, these dimensions were assessed using the *DraftSight*® software.

2.3.2. Eddy current non-destructive testing

Eddy current non-destructive testing was conducted on sample d) (Fig. 1) of HSLA steel parts manufactured with the parameters described in Table 3. For this purpose, the cutting surface of the samples was grounded and polished to obtain a homogenous surface condition. An experimental setup including an *Olympus* pencil probe operating at 100 kHz and 300 kHz and an *Olympus Nortec 500c* was used, as well as a designed *LabView*® program for data acquisition. Measurements were conducted along the samples' height, and the probe lift-off was held constant, to assess the magnetic permeability of the parts as this has a dominant effect over electrical conductivity given the ferromagnetic nature of the HSLA steels.

2.3.3. Potential drop measurements

Potential drop measurements were performed to assess the electrical conductivity of the HSLA steel parts along its height by using the four-

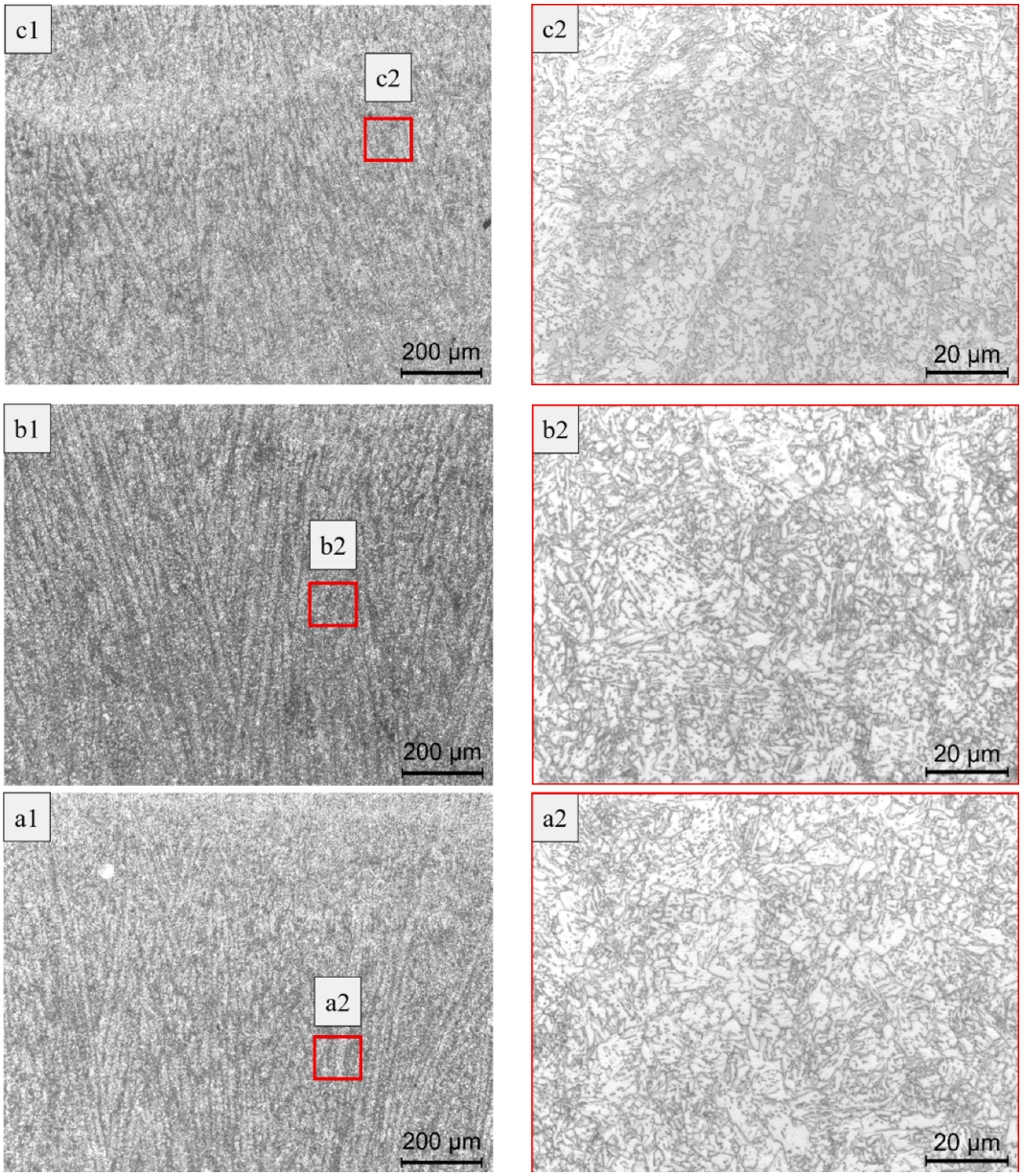

Fig. 6. Microstructure observations of low heat input samples in different wall regions, 10x and 100x magnification, left and right, respectively.

point probe method. Measurements were carried out along 100 mm, spaced by 0.4 mm. A standard *Jandel*^{TM} four-point probe was used with a needle spacing of 654 µm and an imposed current of 80 mA between the external needles using a *2450 SourceMeter SMU Instrument*. The advantage of this technique when compared to that described in section 2.3.2 is that the four-point probe measurements only depend on the electrical conductivity of the material, while the former also considers the magnetic permeability of the material. Furthermore, the electrical conductivity is also related with the materials microstructure and microhardness [37].

2.3.4. Macro and microstructural characterization

The properties of a given alloy depend on the corresponding chemical composition and the processing that it was subjected, i.e., its thermal and mechanical history. These aspects inflict a given microstructure on the material and will influence its final mechanical properties. In this way, microstructure analysis was performed to evaluate the different metallurgical aspects inherent to this manufacturing process as a result of the layer-by-layer deposition, such as steel phases, grain size and morphology variations along the building direction. For this purpose, samples were obtained from the bottom (a), middle (b) and upper (c) regions of the thin-walled HSLA steel parts using a *GBS-218 Eco AutoCut* saw machine, mounted in epoxy resin, grounded and polished following standard metallographic procedures and then etched in Nital (10% solution). Samples were then observed on a Leica DMI 5000 M inverted optical microscope.

2.3.5. Microhardness measurements

Microhardness measurements were performed using a Mitutoyo HM-112 microhardness tester on polished and etched samples d) of the HSLA steel parts, according to ISO Standard 6507–1:2018. A load of 1 kgf was applied for 10 s, along a height of 100 mm from the bottom to the top of the sample. The spacing between consecutive indentions was 0.5 mm.

2.3.6. Uniaxial tensile testing

Uniaxial tensile specimens were produced by electrical discharge machining using an ONA AF35 machine. Their geometry and dimensions were established according to standard ASTM E8 / E8M-13a

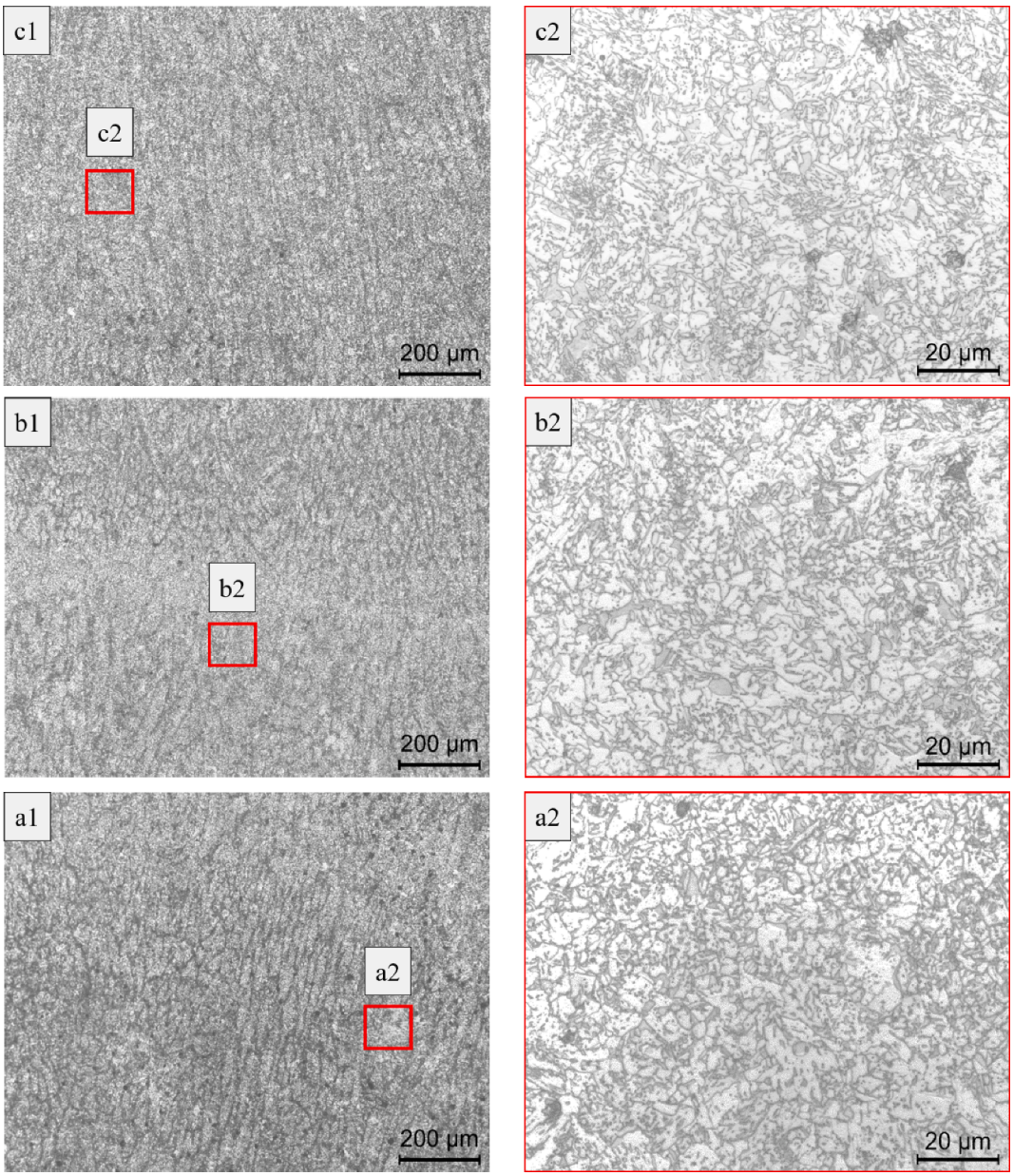

Fig. 7. Microstructure observations of high heat input samples in different wall regions, 10x and 100x magnification, left and right, respectively.

and are presented in Fig. 2. Width and thickness of all specimens were measured to determine the nominal cross-sectional area.

Tests were carried out at room temperature using specimens from three low heat input walls and three high heat input walls, on an electromechanical *Instron*® testing machine with a load capacity of 50 kN. Additionally, strain was measured using a clip-gauge extensometer with a gauge length of 25 mm. The Video Image Correlation (VIC) optical technique was used on the testing of two samples (1L and 4H), in order to obtain a full strain data distribution with higher accuracy. All tests were performed under a cross-head speed of 1 mm/min.

2.3.7. *Fatigue testing*

As higher cooling rates promote the nucleation of acicular ferrite solid solution which is associated with better mechanical properties, namely yield and tensile strength, low heat input samples were selected to undergo fatigue testing. Therefore, nine specimens were extracted from three thin-walled HSLA steel parts. Specimens were designed according to standard ASTM E466-15, and their geometry and dimensions are depicted in Fig. 3. Specimens were extracted by electrical discharge machining.

Prior to fatigue testing, specimens' surface roughness was measured using a MarSurf PS10 portable device and dye penetrant testing was performed on all specimens to identify any surface-breaking defects.

Fatigue tests were performed at room temperature, on a servo-hydraulic *Instron® 8502* testing machine with a load cell of 100 kN. A load-controlled regime, with a stress ratio of 0.1 ($R = 0.1$), and sinusoidal constant amplitude with frequency between 12 Hz and 15 Hz was employed. Tests were carried out until specimen's fracture or until they reached 2×10^6 cycles, which were then stopped and considered as run-out. Additionally, a clip-gauge extensometer was placed in the last tested specimen in order to record the strain behaviour with respect to the imposed loading conditions.

After testing, selected fracture surfaces were observed in a Jeol JSM-7001F FEG-SEM equipped with energy dispersive spectrometry (EDS), to analyse their morphology, the crack initiation region, and the crack propagation mechanisms.

Fig. 8. Schematic representation of the cooling flow (arrows indicate the cooling direction).

3. Results and discussion

3.1. Macroscopic characterization and microstructure

The fastest travelling speed used to produce the low heat input samples led to lower dilution as well as lower penetration between each layer. This resulted in thinner parts compared to high heat input samples. A lower speed with the same process parameters gave rise to less penetration in the previously deposited layer, increasing the fusion pool, which in turn resulted in wider samples. The required height was achieved with less layers, approximately 70 compared to 90 observed for low heat input samples, which contributed to reduce the manufacturing time. With high heat input, despite an increased wettability during lower speeds, a higher waviness was observed, which may be related with the greater material volume present in this variant. The waviness and width average values of each sample type are presented in Table 4.

The cross-section macrostructure of the low heat input samples and the high heat input samples is presented in Fig. 4 and Fig. 5, respectively. From Fig. 6 and Fig. 7 it is possible to observe, with greater detail, the microstructure evolution along the thin-walled part's height for both type of heat input samples.

The main constituents of this HSLA steel are a mixture of gamageneous and alphageneous elements, i.e., elements that increase the interval of austenite (Ni, Mn) and ferrite (Cr, Mo, Si) solid solutions, respectively [38]. Hence, the columnar morphology observed in the micrographs presented in both Fig. 6 and Fig. 7, corresponds to the solidification that took place initially, where the dominating microstructure is austenitic. Subsequent cooling led to ferrite formation from the austenite grain boundaries. This process repeats itself with each adding layer. Therefore, during manufacturing the microstructure experienced back and forth austenite and ferrite transformations. The final microstructure is composed mainly of pearlite and ferrite. In addition, bainite or acicular ferrite are some of the solid solutions that can arise [12]. The nucleation of intragranular acicular ferrite, particularly, contributes to increase the material resistance and toughness [39].

Microstructural analysis showed columnar grains oriented along the building direction with a clear inclination preference towards the centre. This aspect can be explained by the cooling effect that occurred from the edges towards the centre of the wall (Fig. 8). As the layer edge is approached, a remelting zone is visible, resulting in a discontinuity on grain distribution and finer microstructure, e.g. Fig. 7 c1). Depending on the ability of dissipating heat, the columnar grain may present higher or lower width, and this aspect differs from high to low heat input samples.

Within each thin-walled part, all the samples analysed revealed finer microstructure at the bottom and the top when compared to the middle region. Therefore, grain size was observed to increase along the building direction and decrease towards the top region. With each additional

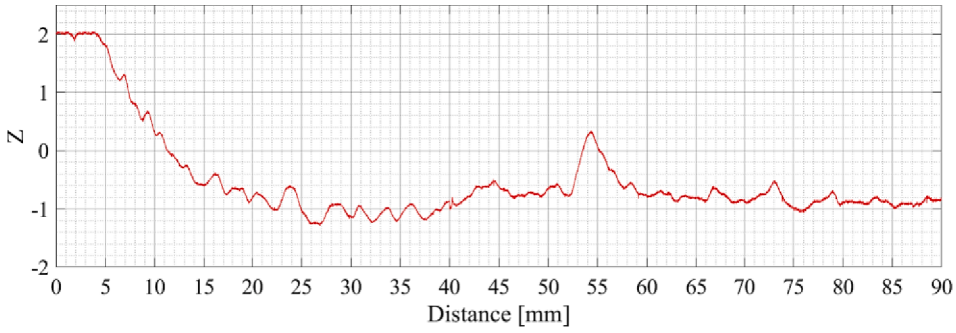

Fig. 9. Eddy current testing results on 5H sample with 300 kHz.

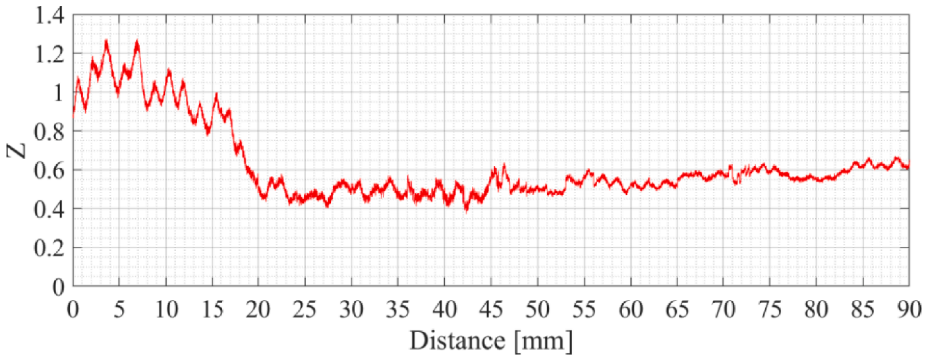

Fig. 10. Eddy current testing results on 3L sample with 100 kHz.

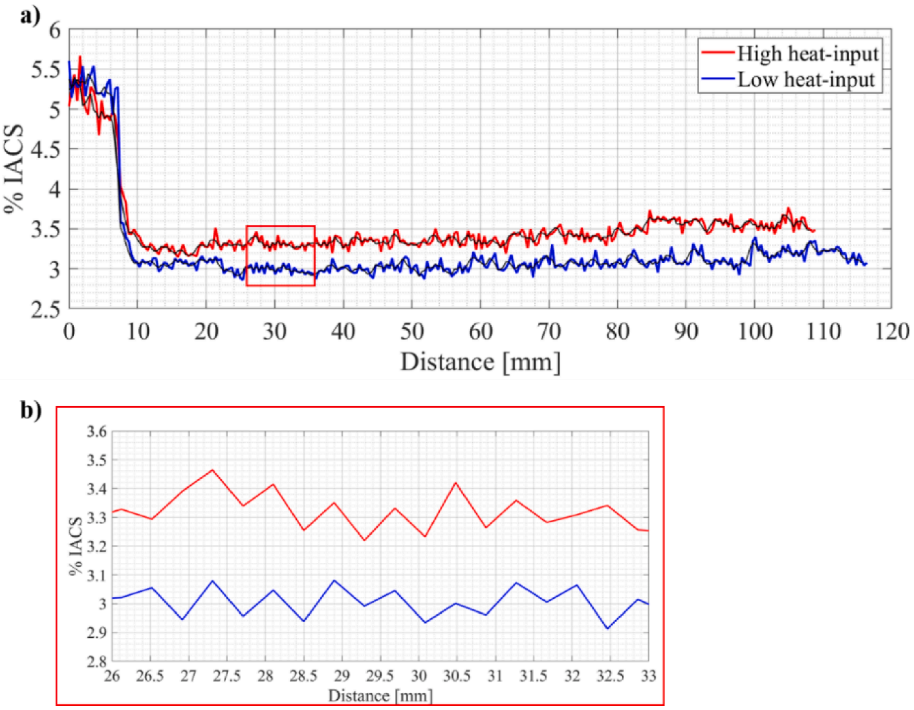

Fig. 11. (a) Electrical conductivity along height and (b) detailed observation of 3L and 6H samples.

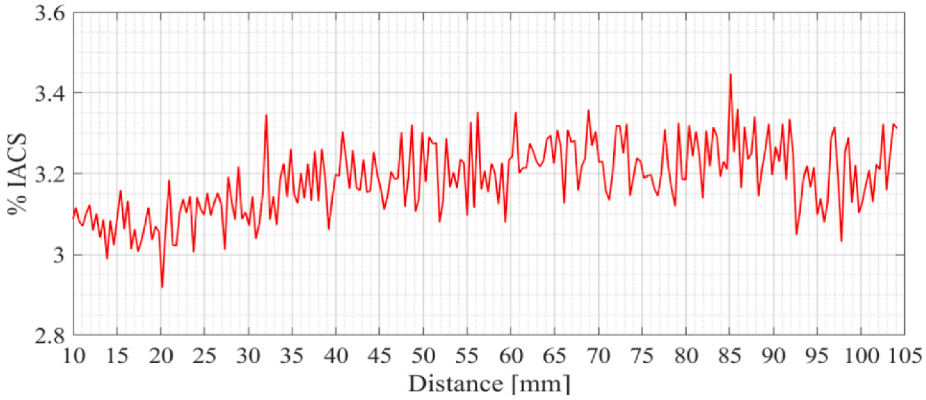

Fig. 12. Electrical conductivity of 5H sample.

layer, the building sample experienced a decrease in thermal cycles, and thus, the temperature in the middle section was kept at a higher level for a longer period of time, which allows to explain the courser grain observed and also reported in [24].

When different heat input microstructures were compared, high heat input samples revealed an overall slight increase in grain size due to the lower cooling rates that these walls were subjected. Additionally, lower heat input is associated with higher cooling rates, which consequently increases heat gradients and leads to finer microstructure compared to high heat input walls. Moreover, cooling rates on both type of samples were not low enough to cause the formation of brittle and hard microstructure such as martensite.

Nonetheless, the grain size increase, on all observed samples, did not seem to be significant, which led to assume that the equal cooling time in between layers may have a more profound effect on grain growth than the heat input. Although layers on high heat input walls always started at a higher temperature, the dwell time influence the extent to which the material is able to accommodate and experience grain growth, as in an equilibrium situation. Another approach to compare different heat input microstructures would be by starting the deposition always at the same temperature despite still having different welding speeds.

3.2. Magnetic permeability and electrical conductivity

The Eddy current tests performed on low heat input samples were more difficult to conduct than those on high heat input samples. The reason that explains such difficulty is the flow distortion experienced due to the edge effect that prevails on the narrow width profile, given that the probe diameter was approximately the same size as the profile width. Nonetheless, a similar trend was observed on both heat input samples regarding its magnetic permeability (Fig. 9 and Fig. 10). From Fig. 10 (low heat input sample), it is possible to observe a clear signal trend as the probe progresses throughout the sample. Given the substrate penetration during the first layer deposition along with the added temperature, a ramp progression is observed instead of an abrupt variation. One may conclude that when compared with the base material, all samples present a lower magnetic permeability. Another conclusion is that in the presence of stable processing conditions, the magnetic permeability tends to remain uniform. However, regarding 5H sample results, presented in Fig. 9, the few substantial variations noted,

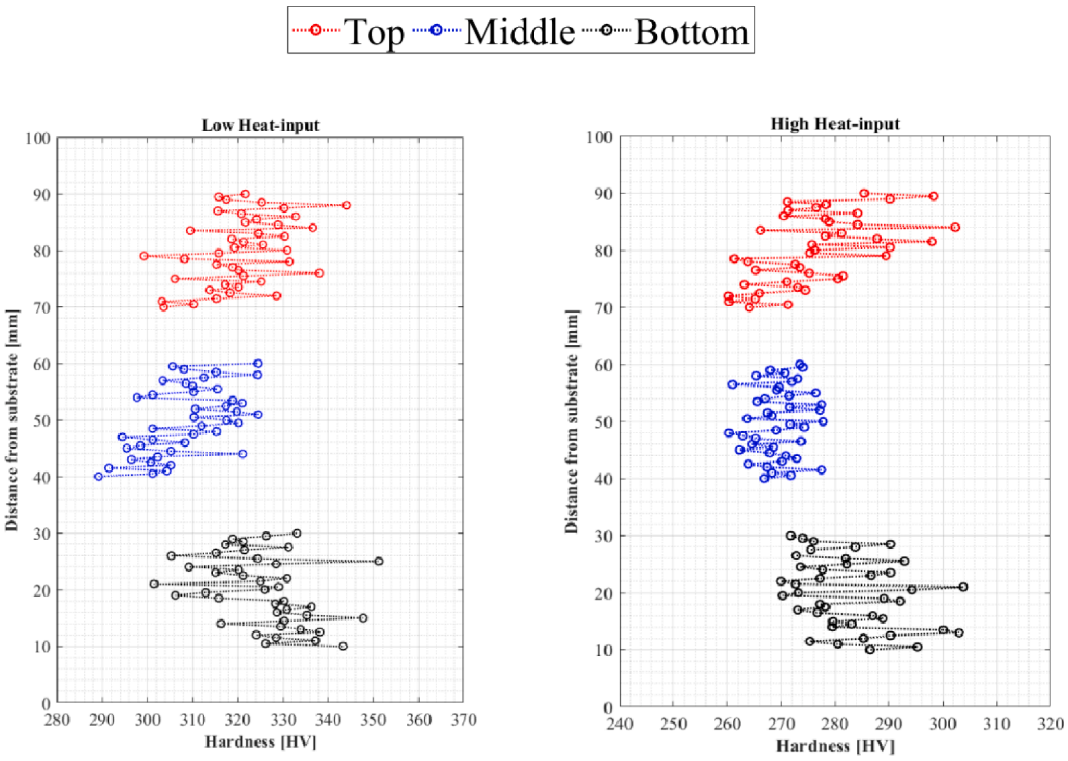

Fig. 13. Microhardness measurements along specimens' height (3L and 4H).

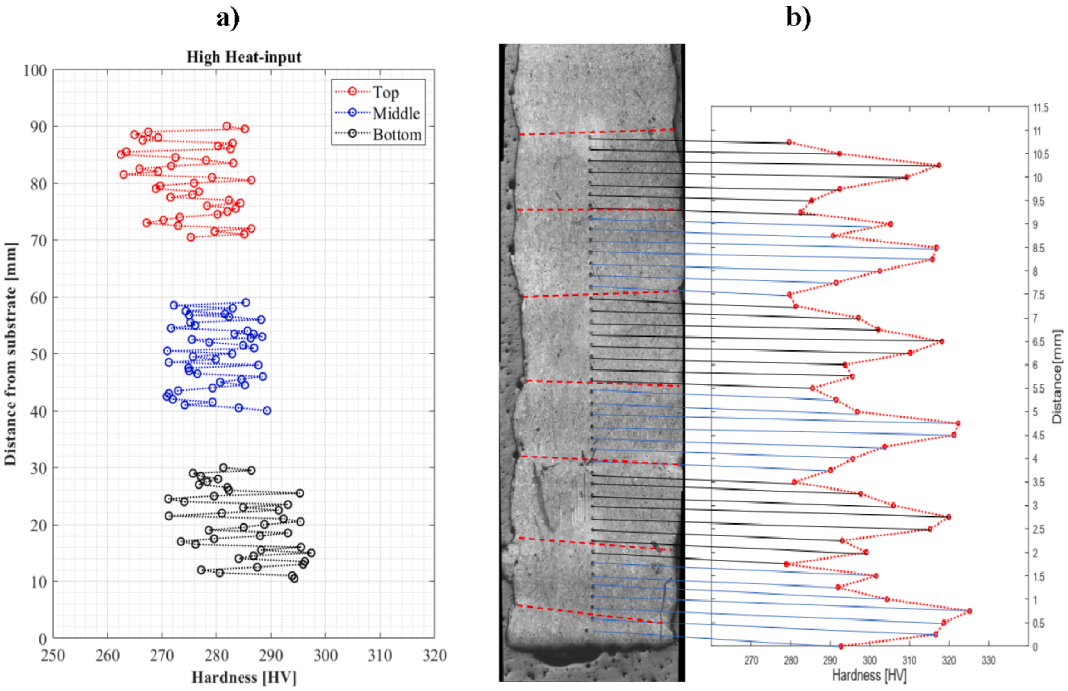

Fig. 14. a) Microhardness profile of 5H sample and b) detailed layer observation of 3L sample.

especially near the 55 mm distance, can be attributed to either a pore defect located on the sub-surface region or to the change of inter-layer cooling time on that particular region. Since during the manufacturing process the machine was interrupted due to technical issues, which could allow for a dwell time higher than one minute, resulting in a longer cooling period, the next layers were then subjected to different temperature conditions which led to changes in the microstructure and consequently on the magnetic permeability of the material.

Fig. 11 shows the electrical conductivity results along both samples height. As expected, a transition was observed as the probe progressed from the substrate towards the first layers, given the heterogeneous properties between the two materials. In addition, low heat input samples demonstrated a lower electrical conductivity profile of about 3% IACS. Such behaviour may be explained due to the fewer thermal cycles these samples were subjected to, which originated a smaller grain size as already observed in section 3.1. High heat input samples see an increase

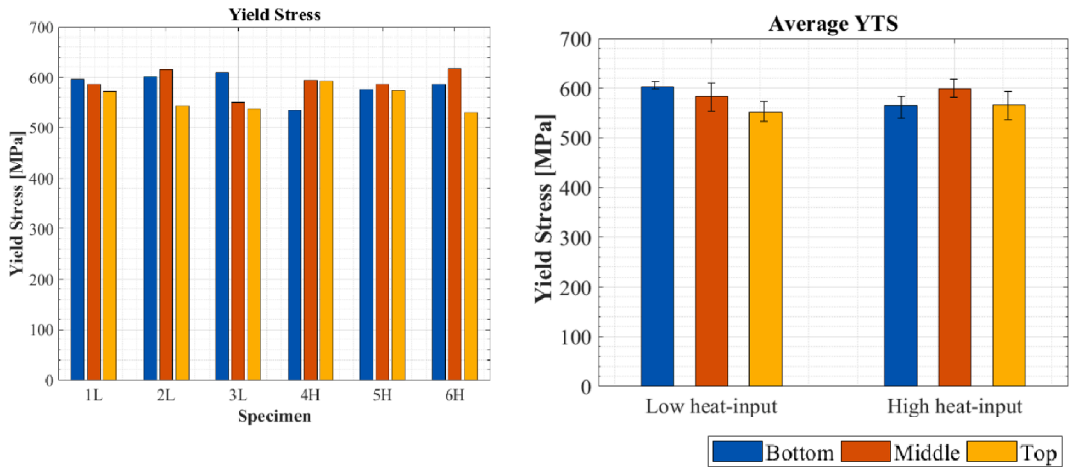

Fig. 15. Yield Stress (YTS) and the corresponding average value (right).

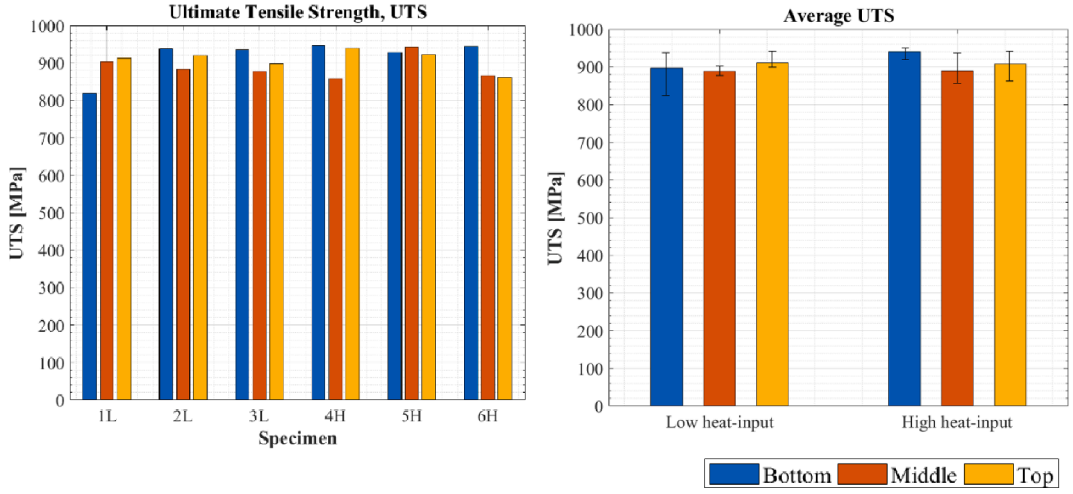

Fig. 16. Ultimate Tensile Strength (UTS) and the corresponding average value (right).

in grain size, with reduced grain boundaries which benefits the electrical current flow. Furthermore, towards the end of both thin-walled parts, a slight increase of electrical conductivity was observed.

Steel's electrical conductivity is known to range between 3 – 15 % IACS. In this case, the HSLA parts showed an average conductivity between 3 – 3.5 % IACS, which is well represented for this type of steels, that generally presents lower electrical conductivity. The presence of 1.7 % of manganese and 2% of nickel are not only responsible for increasing the hardenability, strength, or ductility, but also produce a significant effect on electrical resistivity.

Regarding 5H sample, electrical conductivity results are depicted in Fig. 12. It is possible to detect a slight variation of electrical conductivity, especially from 30 mm distance onwards. Although the small variation may be negligible, it is necessary to take it into account in order to understand the variation observed in Eddy current testing. Four-point probe testing revealed to be a complementary analysis of Eddy current testing when ferromagnetic materials are concerned. Both profiles showed a similar path trend, which allows to conclude that in the presence of uniform conditions during processing and the absence of structural defects, such as pores or inclusions, both magnetic permeability and electrical conductivity do not significantly vary along samples' height, regardless the input energy.

3.3. Microhardness and mechanical properties

Microhardness measurements showed different results as far as energy input is concerned. Low heat input samples presented a harder microstructure (327 ± 14 HV1.0) than high heat input samples (277 ± 9 HV1.0). This result may be explained by the increase in heat accumulation and larger grain size present in the latter. Moreover, it is possible to observe a visible evolution pattern along the material's height, Fig. 13. All samples start from a higher microhardness value and decrease close to the middle, only to start increasing again near the top. This variation in microhardness values between the different wall regions may be attributed to the effects of thermal histories on the mechanical behaviour [12]. As stated in the literature, the temperature stabilizes from a certain layer that is located near the middle region. In this way, the first layers, the middle and upper regions experience different thermal cycles effects, which influence grain size, as well as phase formation processes. Thus, in uniform process conditions, i.e., exempt of any stops, it is possible to conclude that hardness decrease in the middle section suggests an increase in material ductility due to more pronounced heat accumulation experienced when compared to bottom or top regions.

Following the observations made on the 5H sample on the previous sections, the microhardness profile is represented in Fig. 14a). Contrary to the remaining profiles, this sample does not show a hardness decrease in the middle region or a similar increase in the top region. It is possible

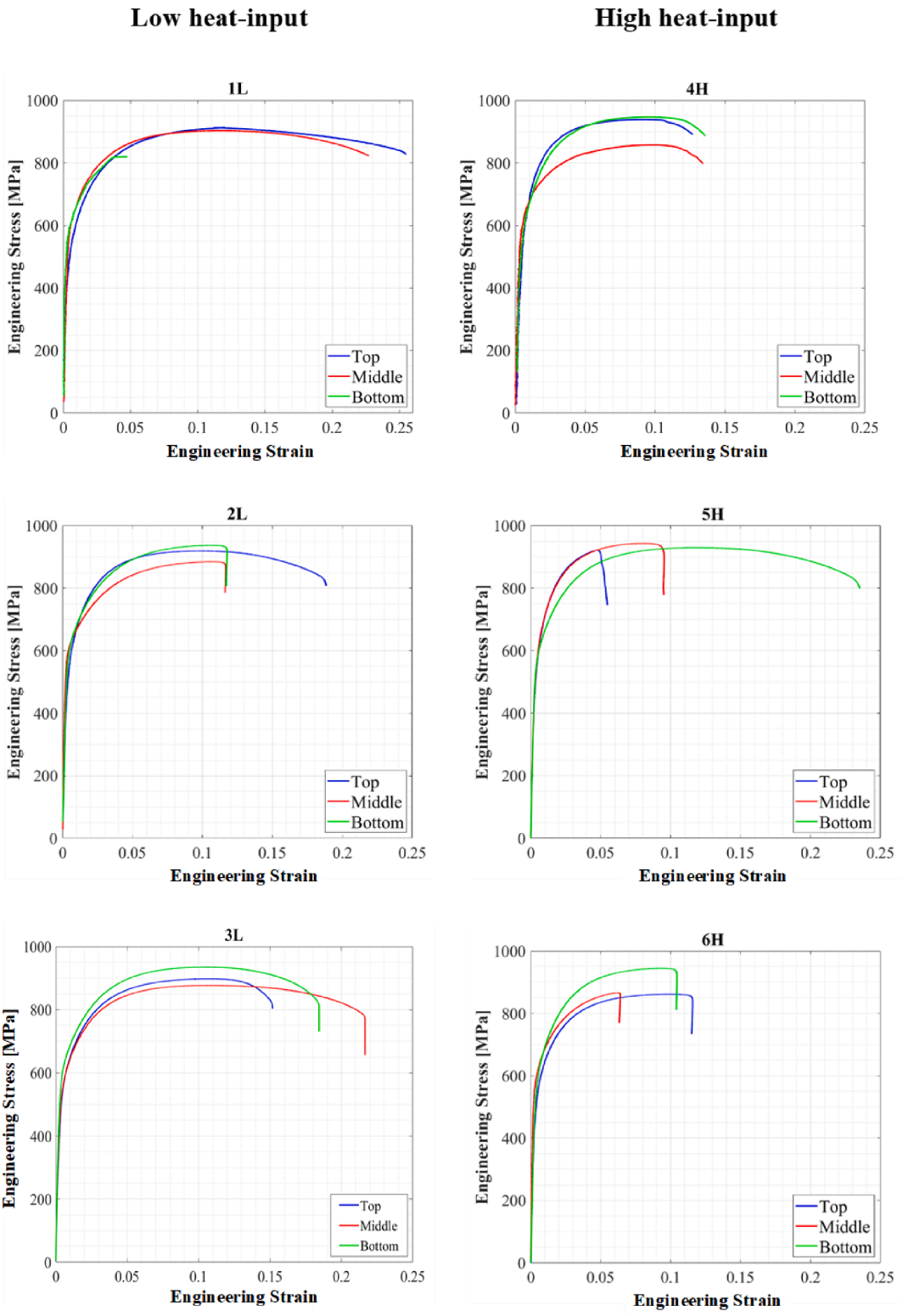

Fig. 17. Stress - Strain curves of low heat input (1L, 2L and 3L) and high heat input (4H, 5H and 6H) specimens.

to conclude that, regardless the existence of a material defect, the different results are a consequence of a change in microstructure due to an increased dwell time in-between layers. The subsequent layers experienced cooler conditions, almost similar to the bottom region, which resulted in smaller grain size and thus, increased hardness.

Another important aspect concerning this testing is the hardness variation along the layer, which is presented in more detail in Fig. 14b) for 3L sample in the middle region. A significant decrease in hardness is visible near the layer boundary. Whereas the maximum hardness value is obtained in the mid layer region. This feature may be explained by the following: after the last deposited layer, the outermost region experiences a faster cooling rate, as displayed in Fig. 8, which resulted in a harder microstructure. However, when the next layer is deposited, it partially remelts the previous one and in addition, it acts as a heat

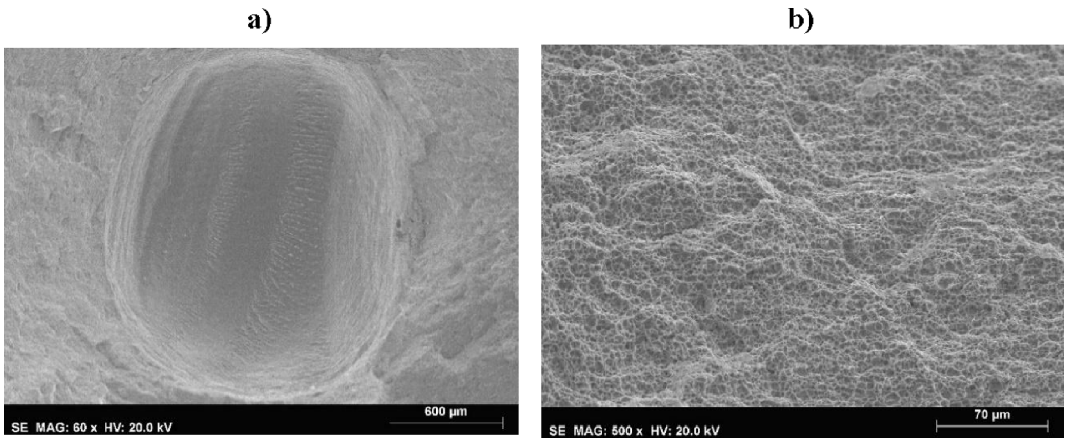

Fig. 18. Fracture surface features of a) 5H top and b) 3L bottom specimens.

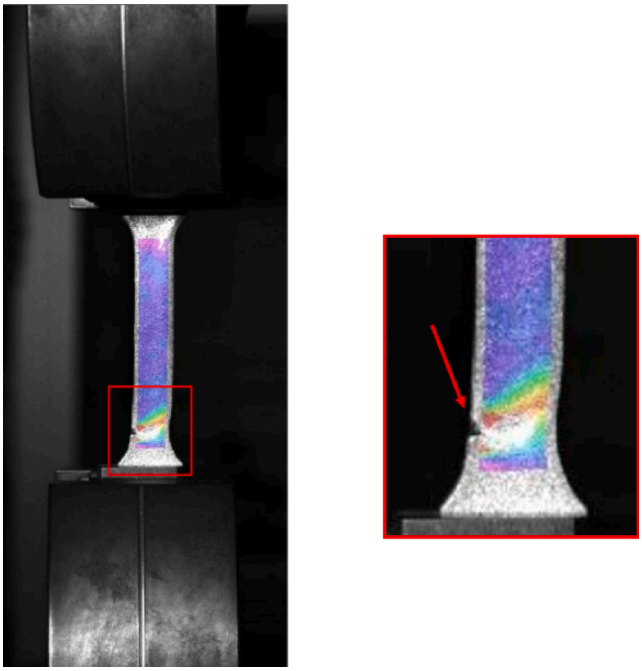

Fig. 19. Identification of a surface pore defect that induced premature fracture on 4H middle specimen.

treatment. This annealing effect causes finer microstructure in that region and decreases the interface microhardness. This is an important aspect to understand, since there is not only variation along the height, but also from layer to layer and within the layer.

After performing the uniaxial tensile tests, all the results were processed in order to obtain the adequate stress-strain curve for each specimen. Given the difficulty to identify the stress at which the material changes from elastic to plastic behaviour, the 0.2% offset yield strength was determined. All specimens presented a ductile fracture due to an increased plastic deformation with a subsequent decrease in cross-sectional area. Ultimate tensile strength (UTS) values ranged between 860 MPa – 950 MPa, which was similar to material's specification [34], 940 MPa – 980 MPa. Data sheet values for yield tensile stress (YTS) present a range of 880 MPa – 920 MPa, however, the results obtained from the tests were considerably lower, 530 MPa – 620 MPa, resulting in an average decrease of 35 %. YTS and UTS results can be observed in Fig. 15 and Fig. 16, respectively.

It is important to note, however, that not all specimens fractured within the clip gauge measuring length, which adds to the conclusion that important elongation was not measured after necking occurred. This aspect was possible to overcome by performing tests using VIC on specimens 1L and 4H.

From Fig. 15 is observed that YTS does not present a significant or straightforward pattern between the different heat input specimens. YTS on low heat input specimens decreased on average along the building direction, whereas on high heat input the middle section presented the higher YTS value. Although it decreased globally compared to the material specification, as mentioned previously, it is not possible to establish a direct relationship between heat input or wall region and the YTS of the material. Although it is possible to observe a decrease along height on low input specimens, this is contradicted by the high input specimens. Another important aspect that potentially masks the results is the presence of surface and internal defects. Thus, as far as these results are concerned, it is possible to assume that YTS does not vary significantly with respect to energy input and wall region.

On the other hand, in average, UTS is slightly higher in the bottom and top tested specimens. This can be explained by the higher hardness of the first and last layers (Fig. 13). As such, the lower value of UTS is found to be in the middle, as expected, following the microhardness profile pattern presented in Fig. 13. Specimens from 3L wall represent very well this characteristic since no significant stops occurred during manufacturing. Contrary to 3L, 5H wall presented a small UTS increase in the middle region (Fig. 16), which is not supported by the microhardness results presented in Fig. 14a). Moreover, from the stress-strain curves presented in Fig. 17, the lower strain displayed by the upper specimen of 5H wall should not be representative of that region, nor the material, since subsequent fracture analysis displayed the presence of pores, which were responsible for the premature fracture, as observed in Fig. 18a). A first look on 3L stress-strain curves shows that greater ductility was achieved in the middle region. Since hardness and ductility are inversely related, it is possible to assign this behaviour to the microhardness profile that was already mentioned. The observations made from this wall agree with the fracture surface analysis, Fig. 18b), which revealed the presence of dimples, denoting ductile fracture.

Nonetheless, it is essential to bear in mind that material hardness should not be the only property to look at. Internal defects, manufacturing conditions or even specimens' preparation should be considered and can also explain the different patterns observed in the stress-strain curves presented in Fig. 17. This aspect was verified on testing using VIC, where 1L top and middle specimens displayed significant elongation due to the absence of any defect. On the other hand, all 4H specimens displayed premature fracture due to surface pores, as indicated by the arrow in Fig. 19.

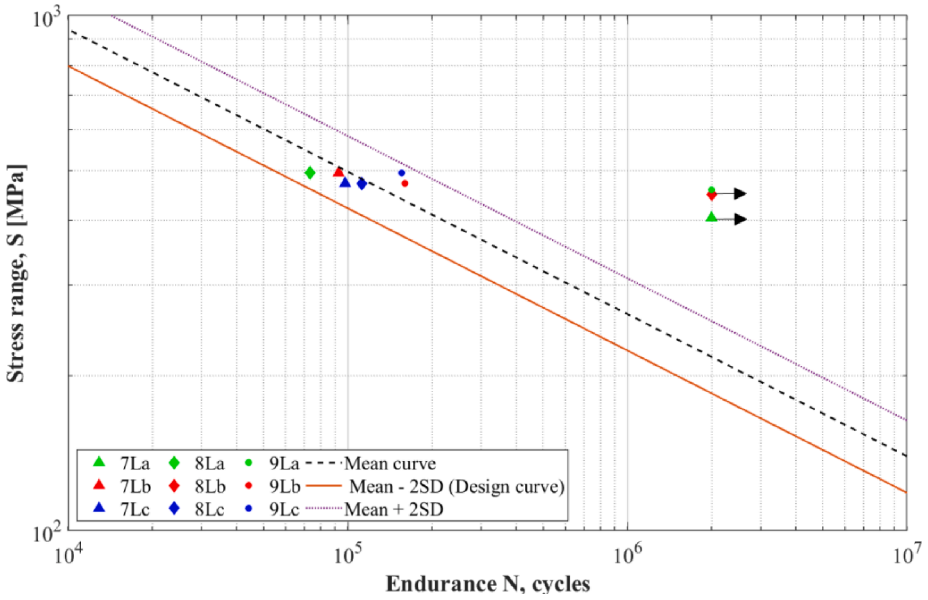

Fig. 20. S-N fatigue curve.

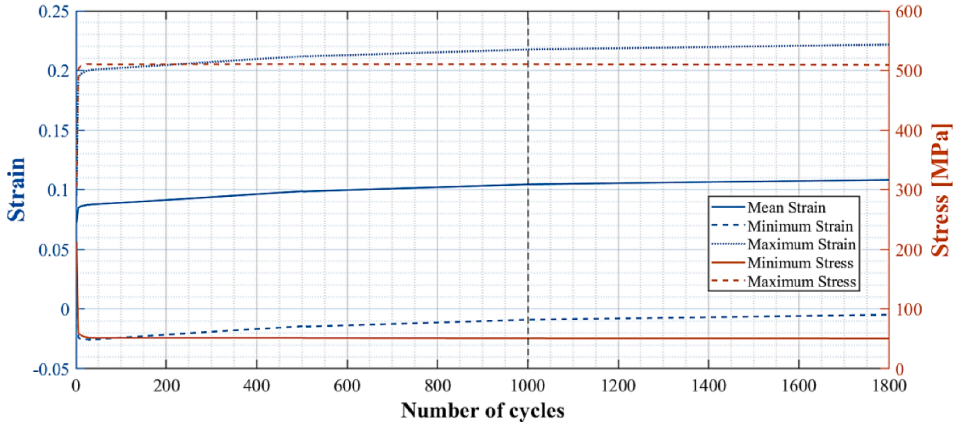

Fig. 21. Stress and strain progression with the number of cycles.

3.4. Fatigue data and fractography analysis

The non-destructive inspection performed by dye penetrant on all fatigue specimens prior testing did not reveal any superficial defects as pores or cracks, that would otherwise generate stress concentration and lead to premature crack initiation.

After testing regression analysis was used to determine the mean and design curves of the experimental data. The mean S-N curve was obtained using equation (1) assuming N_f as the dependent variable. The correlation line fitted by equation (1) represents the average regression curve with 50% of probability of failure. The regression line is expressed by equation (2) in logarithmic notation, where S represents the stress range, N_f is the number of cycles to fracture, C is the fatigue strength coefficient and m is the fatigue strength exponent or the slope of the S-N curve. C and m are empirical constants, calculated from the experimental data. The results for C and m were 5.76×10^{14} and 3.62, respectively. The S-N curve is plotted in a log-log scale in Fig. 20.

$$S^m \bullet N_f = C \tag{1}$$

$$log(N_f) = log(C) - m \bullet log(S) \tag{2}$$

Additionally, the normal distribution is represented, symmetrical to the mean curve and is quantified by the standard deviation (SD), according to BS 7608:2014. Future fatigue data points are predicted to occur in-between the design curves, also known as confidence limit. According to the aforementioned standard, there is a failure probability of 2.3% below the design curve (mean curve – 2SD). The SD of the data was 0.127. Fatigue strength at 10^6 cycles, calculated according to the mean curve, was 263 MPa.

Except for the three specimens that reached two million cycles without failure, the other six fractured within a range between 10^4 and 10^5 cycles. This feature suggests that fatigue testing was very close to Low Cycle Fatigue (LCF) regime. Additionally, strain was observed to be mainly plastic, which is supported by the great ductility of the specimens observed during testing. As such, these observations lead to conclude that strain-controlled instead of load-controlled testing would have been more appropriate and should be adopted in future investigations [40]. In case of strain-controlled testing, stress is an independent variable, and consequently it is easier to assess whether the material suffered dynamic hardening or softening.

The clip-gauge extensometer placed on specimen 9La allowed to assess the strain behaviour during testing. Fig. 21 illustrates the results, where is possible to observe that minimum and maximum stresses remained constant with respect to the number of cycles. However, mean strain continuously increased until near one thousand cycles, from which then remained constant until it reached 2×10^6 cycles. Among

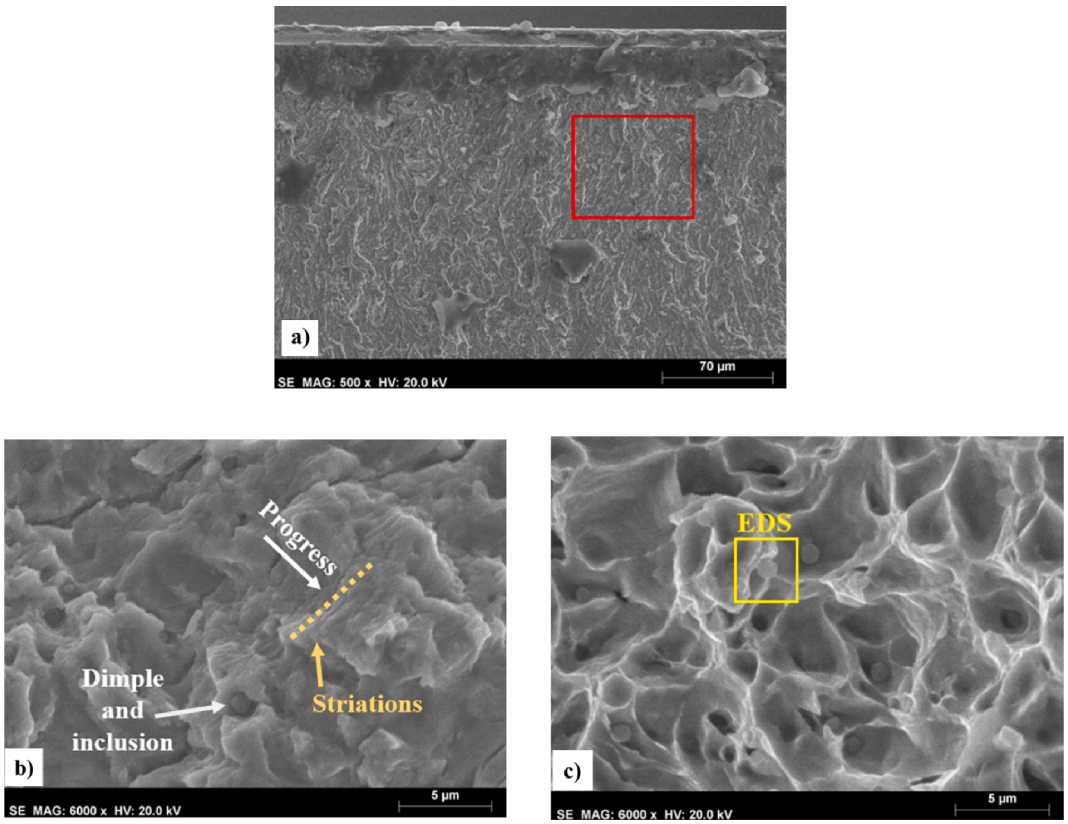

Fig. 22. SEM observations of HSLA steel fracture surfaces of a) 10Lc specimen showing crack nucleation b) 10Lc specimen showing striations and c) 10Lb specimen showing ductile fracture (dimples and inclusions).

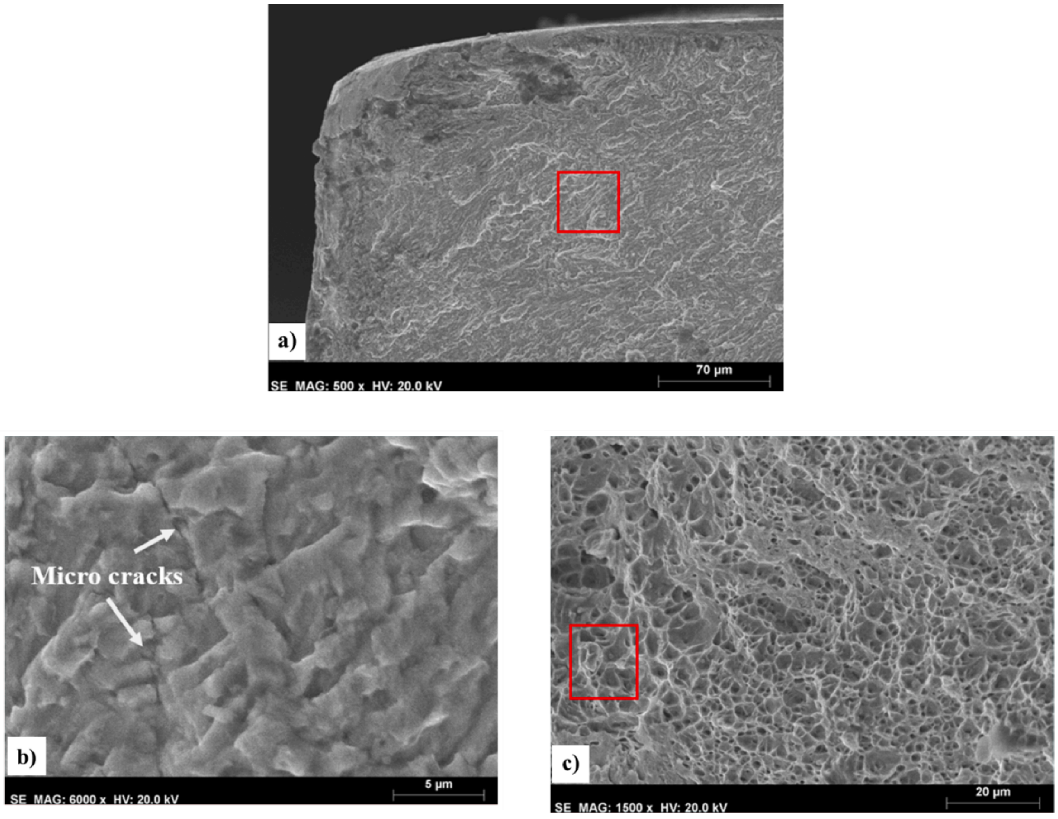

Fig. 23. SEM observations of HSLA steel fracture surfaces of 10Lb specimen showing a) crack nucleation, b) micro cracks and c) ductile fracture (dimples and inclusions).

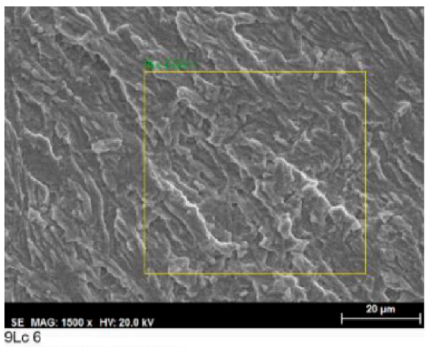

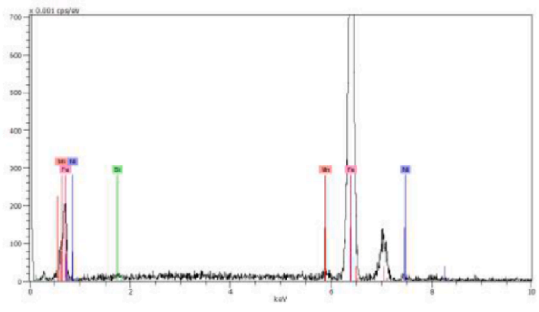

El	AN	Series	unn. C [wt.%]	norm. C [wt.%]	Atom. C [at.%]	Error (1 Sigma) [wt.%]
Fe	26	K-series	211.48	97.58	97.47	6.07
Mn	25	K-series	2.79	1.29	1.31	0.26
Ni	28	K-series	2.13	0.98	0.93	0.29
Si	14	K-series	0.32	0.15	0.29	0.09
Total:			216.72	100.00	100.00	

Fig. 24. EDS analysis on a HSLA fatigue specimen.

the many typical cyclic behaviours, cyclic creep was observed to occur in this particular case, which is associated to force-controlled conditions with unequal force limits ($R \neq -1$). This phenomenon is related to the continuous increase of the mean strain while strain amplitude remains constant [24,40]. In this case, it is difficult to draw a conclusion, since although minimum and maximum strain increased in equal extent before it remained constant (around 1000 cycles), maximum stress was not high enough to produce fracture. This phenomenon, however, still lacks investigation as far as WAAM is concerned, and as such, should be considered in future studies.

Fatigue fracture surfaces observed in a Scanning Electron Microscope (SEM) revealed crack initiation near the edge, which suggests the absence of internal defects, as pores or entrapped inclusions (Fig. 22a) and 23a)). From fracture surfaces analysis, two types of surface crack initiation were observed. Corner quarter-elliptical cracks (Fig. 22), as a result of a geometric discontinuity and semi-elliptical cracks (Fig. 23). Mixed mechanisms of crack propagation occurred. Fibrous fracture initially represented by fatigue striations, where each striation spacing describes the crack progression in each cycle. Crack propagation, in this case, occurred perpendicularly to the maximum stress direction as represented by the arrow illustrated in Fig. 22b) and 23b). Towards the end, the surface presents an irregular aspect which corresponds to a ductile fracture, with the presence of dimples, as displayed in Fig. 22c) and 23c), each accommodating a spherical shape inclusion, that through Energy Dispersive Spectroscopy (EDS) analysis, it revealed a higher Mn content (Fig. 24). Additionally, among the different regions (bottom, middle and top), no difference was observed regarding crack nucleation and propagation (Figs. 22 and 23), which suggests that part's height does not have significant influence on the fatigue behaviour of the produced parts.

4. Conclusions

Thin-walled HSLA steel parts were additively manufactured by WAAM using two different heat inputs. All parts were assessed via non-destructive and destructive testing to evaluate the influence of the process heat input and part's height on the additively manufactured material's properties. It was concluded that manufacturing conditions have a more pronounced effect on mechanical properties than the part's height. Electrical conductivity and magnetic permeability were found to be uniform along height, despite the heat accumulation. Low heat input parts presented a slight electrical resistance increase, relative to high heat input, due to the increased number of grain boundaries that restrict the electrical flow. In normal manufacturing conditions, i.e., without stops, microhardness decreased towards the middle and increased in the last layers and a more pronounced ductile behaviour was observed in the middle region. The YTS decreased 35% on average compared to the wire material datasheet. Fatigue results were consistent along the height and the fatigue strength at 10^6 cycles, based on the mean curve, was 263 MPa. Strain monitoring during fatigue testing revealed cyclic creep behaviour. SEM observations of fatigue fracture surfaces confirmed the ductile behaviour inherent to this material. Fatigue striations and dimples were observed. Two types of surface crack initiation were observed resulting in two crack geometries: corner quarter-elliptical and semi-elliptical cracks.

Declaration of Competing Interest

The authors declare that they have no known competing financial interests or personal relationships that could have appeared to influence the work reported in this paper.

Acknowledgements

The authors acknowledge Fundação para a Ciência e a Tecnologia (FCT - MCTES) for its financial support via project UIDB/00667/2020 (UNIDEMI) and project UIDB/50022/2020 (IDMEC under LAETA). The authors gratefully acknowledge A.J. Maltez - Sociedade Metalúrgica Lda for test specimen machining.

References

[1] Di Nicolantonio M. Advances in Intelligent Systems and Computing 975 Advances in Additive Manufacturing, Modeling Systems and 3D Prototyping; 2019.
[2] Zawadzki P, Zywicki K. Smart product design and production control for effective mass customization in the industry 4.0 concept. Manag Prod Eng Rev 2016;7: 105–12. https://doi.org/10.1515/mper-2016-0030.
[3] Zeng Z, Cong BQ, Oliveira JP, Ke WC, Schell N, Peng B, et al. Wire and arc additive manufacturing of a Ni-rich NiTi shape memory alloy: microstructure and mechanical properties. Addit Manuf 2020;32:101051. https://doi.org/10.1016/j.addma.2020.101051.

[4] Thompson MK, Moroni G, Vaneker T, Fadel G, Campbell RI, Gibson I, et al. Design for Additive Manufacturing: Trends, opportunities, considerations, and constraints. CIRP Annals - Manuf Technol 2016;65(2):737–60.

[5] Suryakumar S, Karunakaran KP. A study of the mechanical properties of objects built through weld- deposition, 2013;227:1138–47. https://doi.org/10.1177/0954405413482122.

[6] Haden CV, Zeng G, Carter FM, Ruhl C, Krick BA, Harlow DG. Wire and arc additive manufactured steel: Tensile and wear properties. Addit Manuf 2017;16:115–23. https://doi.org/10.1016/j.addma.2017.05.010.

[7] Alberti A, Bueno BMP, D'Oliveira ASCM. Additive manufacturing using plasma transferred arc. Int J Adv Manuf Technol 2016;83:1861–71. https://doi.org/10.1007/s00170-015-7697-7.

[8] Oliveira JP, Santos TG, Miranda RM. Revisiting fundamental welding concepts to improve additive manufacturing: From theory to practice. Prog Mater Sci 2020;107:100590. https://doi.org/10.1016/j.pmatsci.2019.100590.

[9] Liu W, Lu F, Wei Y, Ding Y, Wang P, Tang X. Special zone in multi-layer and multi-pass welded metal and its role in the creep behavior of 9Cr1Mo welded joint. Mater Des 2016;108:195–206. https://doi.org/10.1016/j.matdes.2016.06.102.

[10] Ragu Nathan S, Balasubramanian V, Malarvizhi S, Rao AG. Effect of welding processes on mechanical and microstructural characteristics of high strength low alloy naval grade steel joints. Def Technol 2015;11:308–17. https://doi.org/10.1016/j.dt.2015.06.001.

[11] Shao Y, Liu C, Yan Z, Li H, Liu Y. Journal of Materials Science & Technology Formation mechanism and control methods of acicular ferrite in HSLA steels: A review. J Mater Sci Technol 2018;34:737–44. https://doi.org/10.1016/j.jmst.2017.11.020.

[12] Rodrigues TA, Duarte V, Avila JA, Santos TG, Miranda RM, Oliveira JP. Wire and arc additive manufacturing of HSLA steel: Effect of thermal cycles on microstructure and mechanical properties. Addit Manuf 2019;27:440–50.

[13] Rodrigues TA, Duarte V, Miranda RM, Santos TG, Oliveira JP. Current status and perspectives on wire and arc additive manufacturing (WAAM). Materials (Basel) 2019;12(7):1121.

[14] Lewandowski JJ, Seifi M. Metal Additive Manufacturing: A Review of Mechanical Properties. Annu Rev Mater Res 2016;46:151–86. https://doi.org/10.1146/annurev-matsci-070115-032024.

[15] Ermakova A, Mehmanparast A, Ganguly S. A review of present status and challenges of using additive manufacturing technology for offshore wind applications. Procedia Struct Integr 2019;17:29–36. https://doi.org/10.1016/j.prostr.2019.08.005.

[16] Gordon JV, Haden CV, Nied HF, Vinci RP, Harlow DG. Fatigue crack growth anisotropy, texture and residual stress in austenitic steel made by wire and arc additive manufacturing. Mater Sci Eng A 2018;724:431–8. https://doi.org/10.1016/j.msea.2018.03.075.

[17] Bandgar S, Gupta C, Rao G, Malik P, Singh RN, Sridhar K. Fatigue Crack Growth Rate Behaviour of HSLA Steel at Varying Load Amplitudes. Procedia Struct Integr 2019;14:330–6. https://doi.org/10.1016/j.prostr.2019.05.041.

[18] Zhang J, Wang X, Paddea S, Zhang X. Fatigue crack propagation behaviour in wire +arc additive manufactured Ti-6Al-4V: Effects of microstructure and residual stress. Mater Des 2016;90:551–61. https://doi.org/10.1016/j.matdes.2015.10.141.

[19] Gordon J, Hochhalter J, Haden C, Harlow DG. Enhancement in fatigue performance of metastable austenitic stainless steel through directed energy deposition additive manufacturing. Mater Des 2019;168:107630.

[20] Biswal R, Zhang X, Syed AK, Awd M, Ding J, Walther F, et al. Criticality of porosity defects on the fatigue performance of wire + arc additive manufactured titanium alloy. Int J Fatigue 2019;122:208–17. https://doi.org/10.1016/j.ijfatigue.2019.01.017.

[21] Biswal R, Zhang X, Shamir M, Al Mamun A, Awd M, Walther F, et al. Interrupted fatigue testing with periodic tomography to monitor porosity defects in wire + arc additive manufactured Ti-6Al-4V. Addit Manuf 2019;28:517–27. https://doi.org/10.1016/j.addma.2019.04.026.

[22] Smith TR, Sugar JD, Schoenung JM, San Marchi C. Relationship between manufacturing defects and fatigue properties of additive manufactured austenitic stainless steel. Mater Sci Eng A 2019;765:138268. https://doi.org/10.1016/j.msea.2019.138268.

[23] Zhang X, Martina F, Ding J, Wang X, Williams SW. Fracture toughness and fatigue crack growth rate properties in wire + arc additive manufactured Ti-6Al-4V. Fatigue Fract Eng Mater Struct 2017;40:790–803. https://doi.org/10.1111/ffe.12547.

[24] Wächter M, Leicher M, Hupka M, Leistner C, Masendorf L, Treutler K, et al. Monotonic and fatigue properties of steel material manufactured by wire arc additive manufacturing. Appl Sci 2020;10(15):5238. https://doi.org/10.3390/APP10155238.

[25] Xin Haohui, Correia José AFO, Veljkovic Milan, Zhang Youyou, Berto Filippo, de Jesus Abílio MP. Probabilistic strain-fatigue life performance based on stochastic analysis of structural and WAAM-stainless steels. Eng Failure Anal 2021;127:105495. ISSN 1350-6307, https://doi.org/10.1016/j.engfailanal.2021.105495.

[26] Li Yajing, Yuan Yutong, Wang Dexin, Fu Sichao, Song Danrong, Vedani Maurizio, et al. Low cycle fatigue behavior of wire arc additive manufactured and solution annealed 308 L stainless steel. Addit Manuf 2022;52:102688. ISSN 2214-8604, https://doi.org/10.1016/j.addma.2022.102688.

[27] Ermakova A, Ganguly S, Razavi J, Berto F, Mehmanparast A. Experimental investigation of the fatigue crack growthbehavior in wire arc additively manufactured ER100S-1steel specimens. Fatigue Fract Eng Mater Struct 2022;45:371–85. https://doi.org/10.1111/ffe.13598.

[28] Ermakova A, Mehmanparast A, Ganguly S, Razavi J, Berto F. Fatigue crack growth behaviour of wire and arc additively manufactured ER70S-6 low carbon steel components. Int J Fract 2022;235(1):47–59.

[29] Xie Cheng, Wu Shengchuan, Yu Yukuang, Zhang Haiou, Hu Yanan, Zhang Mingbo, et al. Defect-correlated fatigue resistance of additively manufactured Al-Mg4.5Mn alloy with in situ micro-rolling. J Mater Process Technol 2021;291:117039. ISSN 0924-0136, https://doi.org/10.1016/j.jmatprotec.2020.117039.

[30] Liao Zhen, Yang Bing, Xiao Shoune, Yang Guangwu, Zhu Tao. Fatigue crack growth behaviour of an Al-Mg4.5Mn alloy fabricated by hybrid in situ rolled wire + arc additive manufacturing. Int J Fatigue 2021;151:106382. ISSN 0142-1123, https://doi.org/10.1016/j.ijfatigue.2021.106382.

[31] Syed Abdul Khadar, Zhang Xiang, Caballero Armando, Shamir Muhammad, Williams Stewart. Influence of deposition strategies on tensile and fatigue properties in a wire + arc additive manufactured Ti-6Al-4V. Int J Fatigue 2021;149:106268. ISSN 0142-1123, https://doi.org/10.1016/j.ijfatigue.2021.106268.

[32] Wang Xinyan, Zhao Yang, Wang Luobin, Wei Limin, He Jingjing, Guan Xuefei. In-situ SEM investigation and modeling of small crack growth behavior of additively manufactured titanium alloy. Int J Fatigue 2021;149:106303. ISSN 0142-1123, https://doi.org/10.1016/j.ijfatigue.2021.106303.

[33] Akgun Emre, Zhang Xiang, Biswal Romali, Zhang Yanhui, Doré Matthew. Fatigue of wire+arc additive manufactured Ti-6Al-4V in presence of process-induced porosity defects. Int J Fatigue 2021;150:106315. ISSN 0142-1123, https://doi.org/10.1016/j.ijfatigue.2021.106315.

[34] Dratec, DT-X90 MSG -Drahtelektrode, (2017) 16834.

[35] Lopes JG, Machado CM, Duarte VR, Rodrigues TA, Santos TG, Oliveira JP. Effect of milling parameters on HSLA steel parts produced by Wire and Arc Additive Manufacturing (WAAM). J Manuf Processes 2020;59:739–49.

[36] Geng H, Li J, Xiong J, Lin X, Huang D, Zhang F. Formation and improvement of surface waviness for additive manufacturing 5A06 aluminium alloy component with GTAW system. Rapid Prototyp J 2018;24:342–50. https://doi.org/10.1108/RPJ-04-2016-0064.

[37] Sorger GL, Oliveira JP, Inácio PL, Enzinger N, Vilaça P, Miranda RM, et al. Non-destructive microstructural analysis by electrical conductivity: Comparison with hardness measurements in different materials. J Mater Sci Technol 2019;35:360–8. https://doi.org/10.1016/j.jmst.2018.09.047.

[38] Geantă V, Voiculescu I, Stefănoiu R, Rusu ER. Stainless steels with biocompatible properties for medical devices. Key Eng Mater 2014;583:9–15. https://doi.org/10.4028/www.scientific.net/KEM.583.9.

[39] Dirisu P, Ganguly S, Mehmanparast A, Martina F, Williams S. Analysis of fracture toughness properties of wire + arc additive manufactured high strength low alloy structural steel components. Mater Sci Eng A 2019;765:138285. https://doi.org/10.1016/j.msea.2019.138285.

[40] Aleksić V, Milović L, Blačić I, Vuherer T, Bulatović S. Effect of LCF on behavior and microstructure of microalloyed HSLA steel and its simulated CGHAZ. Eng Fail Anal 2019;104:1094–106. https://doi.org/10.1016/j.engfailanal.2019.06.017.